JOURNAL OF GLACIOLOGY

CAMBRIDGE UNIVERSITY PRESS

Detection and Characterization of Discontinuous Motion on Thompson Glacier, Canadian High Arctic, Using Synthetic Aperture Radar Speckle Tracking and Ice-Flow Modeling

Journal:	*Journal of Glaciology*
Manuscript ID	Draft
Manuscript Type:	Article
Date Submitted by the Author:	n/a
Complete List of Authors:	Corti, Giovanni; Simon Fraser University, Earth Sciences Rabus, Bernhard; Simon Fraser University, Engineering Sciences Flowers, Gwenn; Simon Fraser University, Earth Sciences
Keywords:	Arctic glaciology, Remote sensing, Glacier modelling, Ice velocity, Glacier flow
Abstract:	We use speckle tracking of high resolution synthetic aperture radar (SAR) images, along with an intensity-rescaling scheme designed to improve accuracy, to investigate discontinuous motion on Thompson Glacier, Umingmat Nunaat, Arctic Canada. The rescaling scheme is developed using simulated SAR images with a known motion field and results in ~25% improvement in speckle tracking accuracy. InSAR and speckle tracking using high resolution RADARSAT-2 data indicate velocity discontinuities of up to 1 cm/d across deep and longitudinally extensive supraglacial channels on Thompson Glacier. We use a cross-sectional finite-element ice-flow model to determine the conditions under which

	velocity discontinuities of the observed magnitude and signature are possible. The modeling suggests that discontinuous motion across (long and straight) supraglacial channels can occur without ice fracture and under a wide variety of glacier thermal structures, including in fully temperate glaciers. Despite the wide range of conditions conducive to discontinuous motion, the form we observe requires that the associated channels be deep, longitudinally extensive and located in regions of lateral shearing. We speculate that these combined conditions are rare except on polythermal glaciers, where drainage features such as moulins are comparatively scarce and lower deformation rates allow channels to incise consistently and persist over many years.

Detection and Characterization of Discontinuous Motion on Thompson Glacier, Canadian High Arctic, Using Synthetic Aperture Radar Speckle Tracking and Ice-Flow Modeling

Giovanni CORTI,[1] Bernhard RABUS,[2] Gwenn E. FLOWERS[1]

[1]*Department of Earth Sciences, Simon Fraser University, Burnaby, BC, Canada*

[2]*Department of Engineering Sciences, Simon Fraser University, Burnaby, BC, Canada*

Correspondence: Giovanni Corti <gcorti@sfu.ca>

ABSTRACT. We use speckle tracking of high resolution synthetic aperture radar (SAR) images, along with an intensity-rescaling scheme designed to improve accuracy, to investigate discontinuous motion on Thompson Glacier, Umingmat Nunaat, Arctic Canada. The rescaling scheme is developed using simulated SAR images with a known motion field and results in ~25% improvement in speckle tracking accuracy. InSAR and speckle tracking using high resolution RADARSAT-2 data indicate velocity discontinuities of up to 1 cm d^{-1} across deep and longitudinally extensive supraglacial channels on Thompson Glacier. We use a cross-sectional finite-element ice-flow model to determine the conditions under which velocity discontinuities of the observed magnitude and signature are possible. The modeling suggests that discontinuous motion across (long and straight) supraglacial channels can occur without ice fracture and under a wide variety of glacier thermal structures, including in fully temperate glaciers. Despite the wide range of conditions conducive to discontinuous motion, the form we observe requires that the associated channels be deep, longitudinally extensive and located in regions of lateral shearing. We speculate that these combined conditions are rare except on polythermal glaciers, where drainage features such as moulins are comparatively scarce and lower deformation rates allow channels to incise consistently and persist over many years.

INTRODUCTION

One of the most glaciologically useful advances in remote sensing has been the advent and proliferation of civilian satellite-based synthetic aperture radar (SAR). SAR, which was first applied as a glaciological tool in 1993 to measure the velocities and grounding line positions of Antarctic ice streams (Goldstein and others, 1993), allows for remote sensing of glacier motion regardless of daylight or weather conditions (Joughin and others, 2011). Furthermore, as the radar is phase sensitive, interferomteric SAR (InSAR) techniques can be applied to resolve glacier motion at the centimeter scale, regardless of the spatial resolution (essentially the pixel size) of the sensor (e.g., Goldstein and others, 1993; Gray and others, 1998). Due to its accuracy, InSAR has been used to measure and investigate "mesoscale" glacier phenomena that result in subtle (i.e., centimeter-scale) perturbations in surface ice velocity fields, such as migration of subglacial water pockets (Fatland and Lingle, 2002) or movement of ice-shelf grounding lines (Rignot, 1998; Rabus and Lang, 2002).

However, while InSAR delivers high resolution deformation measurements, it is only sensitive to motion in the line-of-sight (LOS) direction of the radar and is plagued by a number of complex pitfalls stemming from the cyclical nature of phase data (Yu and others, 2019). Thus, Gray and others (1998) introduced a second SAR-based technique know as speckle tracking that avoids many of the InSAR pitfalls while also measuring motion along both axes of the SAR image. However, unlike InSAR, the accuracy of SAR speckle tracking is linked to the pixel size of the image (Gray and others, 2001; Bamler and others, 2009) and early SAR sensors suffered from coarse spatial resolutions, with pixel sizes on the order of 10 m or larger. Thus, for a number of years, researchers were often forced to choose between InSAR, which was directionally limited and complex, or the simpler and more versatile, but much lower resolution, speckle tracking.

The spatial resolution of SAR sensors has increased significantly since the early 1990s, particularly through introduction of sub-meter resolution spotlight modes, which now allow SAR speckle tracking to approach the resolution of (regular, stripmap mode) InSAR. However, high resolution SAR speckle tracking, which is able to resolve mesoscale glacier motion, remains a relatively under-exploited tool, generally only being used to measure glacier- or ice-sheet-wide velocity fields, albeit at higher resolutions.

Spatially discontinuous glacier motion, which is poorly understood, in part due to a lack of observational evidence, is one form of glacier motion that can now be measured using high resolution speckle tracking. Discontinuous glacier motion generally results from the brittle failure and fracture of ice and can lead to glacier velocity fields that are spatially or temporally discontinuous (e.g., serac fall or glacier collapse).

Discontinuous glacier motion also results in a variety of glacier structures such as crevasses and seracs and can significantly contribute to glacier dynamics (Colgan and others, 2016; Faillettaz and others, 2015).

Speckle tracking

Single Look Complex (SLC) images, essentially SAR images with minimal processing applied post-focusing, exhibit a characteristic speckle pattern. This speckle pattern is controlled by the roughness of the glacier surface at the sub-pixel scale and can be tracked between SLCs, provided that the glacier surface remains relatively unchanged (i.e., has non-zero interferometric coherence), as the speckle pattern is advected downglacier (Moreira and others, 2013; Joughin, 2002). Speckle tracking itself is done by selecting a multi-pixel chip of fixed shape from an initial SAR image and searching for a matching chip in a subsequent image using the normalized two-dimensional (2-D) cross-correlation coefficient (NCC) as a similarity measure. The NCC is generally calculated using the normalized product of SAR image intensities, but in some cases, the interferometric phase is included and this then makes the similarity measure to be optimized equal to the (intensity weighted) interferometric coherence (Joughin, 2002; Gray and others, 2001; Michel and Rignot, 1999). In theory, for featureless areas, phase-based SAR speckle tracking is more accurate than its intensity based counterpart, but is more computationally expensive and requires accounting for systemic phase differences due to factors such as topography (Bamler and Eineder, 2005; De Zan, 2014). Thus, in real-world scenarios, phase-based speckle tracking is used less frequently and may not outperform intensity speckle tracking. It is important to note, however, that phase-based speckle tracking and intensity speckle tracking are fundamentally linked, as a variation in coherence (i.e., decreases in complex cross-correlation due to changing radar scatterers) will lead to corresponding differences of the speckle pattern between chips as the spatial signature of the pattern is ultimately controlled by the phase and amplitude response of the radar scatterers within the resolution cell.

A major benefit of SAR speckle tracking is that it is able to unambiguously resolve glacier motion and benefits greatly from high resolution SAR images as its accuracy is directly linked to pixel size. Moreover, the coherence (i.e., similarity resulting from an unchanged ground/glacier surface) of a scene pair is often better preserved with high resolution SAR images (e.g., Mohammadimanesh and others, 2018) as smaller pixels are less likely to capture an altered radar scatterer (Closson and Milisavljevic, 2017). Thus high resolution speckle tracking presents a powerful, but underleverged, tool for investigating ice dynamics associated with meso-glacier glacier motion. In this study, we develop an intensity prefilter for

SLCs designed to improve the performance of high resolution SAR speckle tracking and use this improved method, in conjunction with a 2-D cross-sectional ice-flow model, to investigate unusual hypothesized mesoscale discontinuous glacier motion (Rabus, 2017) on Thompson Glacier, Canadian High Arctic.

Study site

The study site is located at the head of Expedition Fjord on Umingmat Nunaat (Axel Heiberg Island) in the Canadian Arctic Archipelago (Fig. 1). The Expedition Fjord glaciers include White Glacier, an ~14 km long polythermal glacier that terminates near the head of the fjord. White Glacier ranges from approximately 1800 to 100 m a.s.l. and is one of the most intensively studied (e.g., Hambrey and Müller, 1978; Blatter, 1987; Cogley and others, 1996; Thomson and others, 2017) glaciers in the Canadian Arctic due, in large part, to its proximity to the McGill Arctic Research Station (Thomson and Copland, 2017). Potential evidence of thrust faulting, a controversial form of discontinuous glacier motion (Moore and others, 2010; Monz and others, 2022), has been observed on White Glacier, near the terminus, in the form of "[t]hin, low-angle layers of debris-rich ice" that are often separated from adjacent layers of clean ice by a discontinuous surface (Hambrey and Müller, 1978).

Near its terminus, White Glacier converges with the largest of the Expedition Fjord glaciers, Thompson Glacier, an outlet glacier of the Mueller Ice Cap (Müller, 1962). Thompson Glacier has several named tributary glaciers including Piper (formerly Wreck) Glacier and Astro Glacier. Compared to White Glacier, relatively few glaciological studies have been conducted on Thompson Glacier although several studies have focused more generally on the glaciers of Umingmat Nunaat (Thomson and others, 2017; Müller, 1962; Cogley and Adams, 2000). Mapping of the Expedition Fjord glaciers shows that, between 1948 and 1995, Thompson Glacier advanced approximately 950 m while White Glacier retreated 250 m. The reason for this difference remains unclear, but researchers speculate that differing response times to climatic forcings due to size differences or a slow surge on Thompson Glacier may be responsible (Cogley and others, 2011).

Interferograms generated using RADARSAT-2 data show broken fringes on Thompson Glacier near the White–Thompson confluence and the Piper–Thompson confluence during the winters of 2013 and 2014 (Rabus, 2017). These broken fringes, which resemble those sometimes observed in SAR interferograms of strike–slip earthquakes (e.g., Kobayashi and others, 2018), are potentially indicative of discontinuous motion although the exact nature and cause of the hypothesized discontinuous motion on Thompson Glacier is unclear.

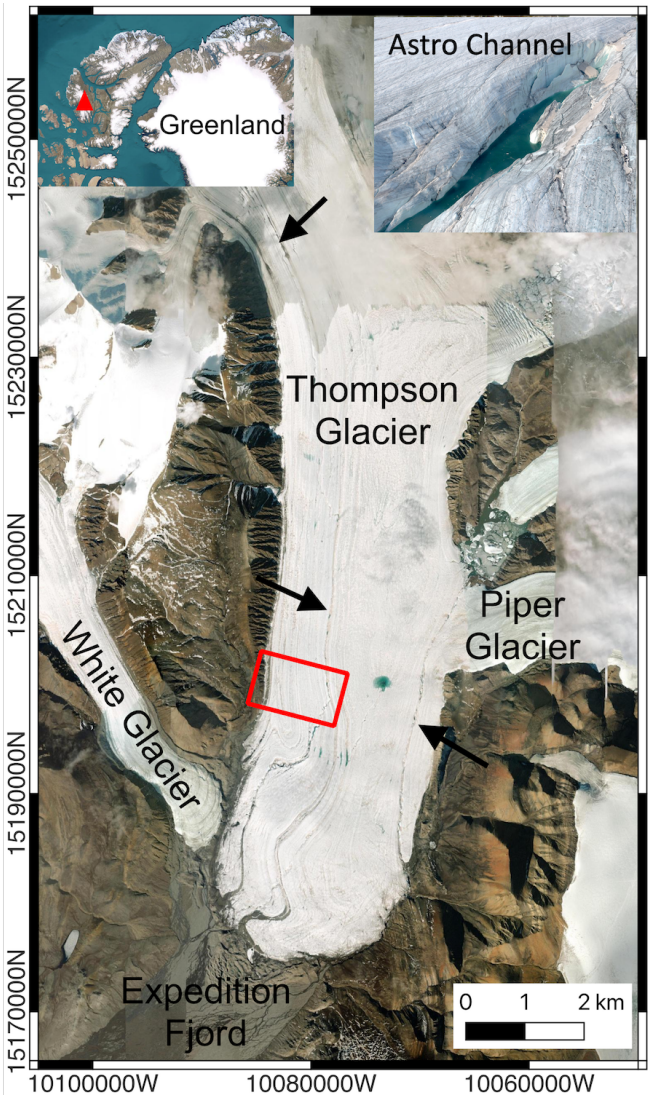

Fig. 1. Study site. Expedition Fjord glaciers on Umingmat Nunaat (Axel Heiberg Island), including Thompson Glacier, the subject of this study. The red box indicates the footprint used in developing the intensity rescaling scheme. The arrows indicate, from top to bottom, the Upper Channel, West Channel and Astro Channel across which discontinuous glacier motion is suspected to occur. Coordinates are given in UTM, Zone 15 N. The inset at top right shows the Astro Channel in 2022 near the Piper-Thompson Confluence. Astro Channel imagery courtesy of Laura Thomson and satellite imagery courtesy of Esri World Imagery (Esri, 2022).

REMOTE SENSING METHODS AND DATA

SAR data

We use SAR speckle tracking to measure the surface velocities of the Expedition Fjord area glaciers with a specific emphasis on the location near the Piper–Thompson confluence. SAR data used in this study (see Table S1) are collected with the spotlight beam mode of RADARSAT-2, a Canadian Space Agency SAR satellite with a 24-day repeat orbit, that operates at C-Band (5.6 cm wavelength) (Van Wychen and others, 2018; Morena and others, 2004). These SAR images have pixel sizes of 1.330–1.332 m in range and 0.379–0.414 m in azimuth. The spotlight beam mode itself employs electronic beam steering to dwell on the area of interest for a longer duration than would otherwise occur, resulting in the high image resolution in the satellite flight (i.e., azimuth) direction as compared to other imaging modes (MDA, 2018). The SAR data are generally collected during the winter and spring as lower temperatures and snowfall help maintain glacier surface coherence, a prerequisite for accurate InSAR and SAR speckle tracking.

False matches due to high intensity pixels

Glacier speckle tracking results often contain rectilinear artifacts (see Fig. 2)—which are clearly non-physical owing to their geometry—that are the result of the speckle tracking algorithm "locking-on" to various features. Here we investigate the underlying cause of these rectilinear artifacts and develop a compensating method to improve the accuracy of speckle tracking.

At its core, speckle tracking identifies similar areas in two consecutive SAR images using the normalized cross-correlation (NCC), which can be written

$$NCC = \frac{\sum_{x,y}[f(x,y) - \bar{f}_{x_0,y_0}][g(x-x_0, y-y_0) - \bar{t}]}{\sqrt{\sum_{x,y}[f(x,y) - \bar{f}_{x_0,y_0}]^2 \sum_{x,y}[g(x-x_0, y-y_0) - \bar{t}]^2}}, \quad (1)$$

where $f(x,y)$ and $g(x,y)$ are the intensity values of the chips being compared, (x_0, y_0) represents the coordinate translation between images, $\bar{t}$ is the mean intensity of the selected chip and $\bar{f}_{x_0,y_0}$ is the mean value of the region in $f(x,y)$ that is being searched (Yoo and Han, 2009). Equation (1) involves element-wise multiplication of the demeaned intensities of the two pixels in the same in-chip position. This makes the NCC particularly sensitive to situations in which high intensity pixels are in the same in-chip position, an issue that is compounded by the strong right-skew of a Rayleigh intensity distribution characteristic of

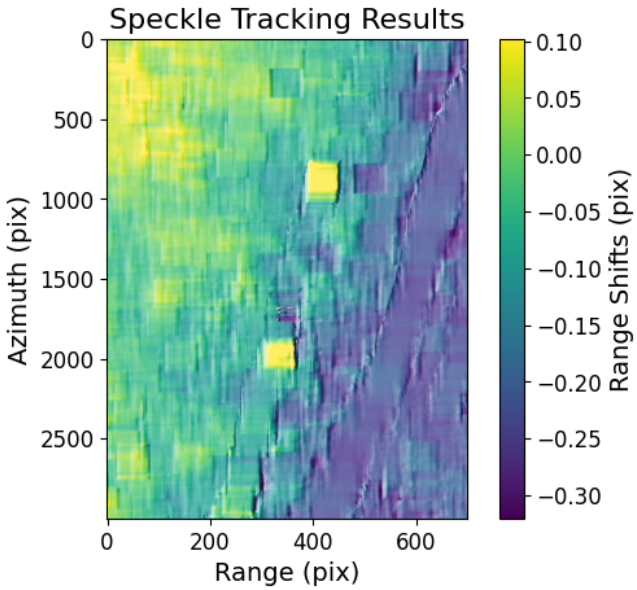

Fig. 2. Hillshaded (30× vertical exaggeration) SAR speckle tracking results (for range direction only) from SLCs collected on 5 January 2022 and 29 January 2022 over Thompson Glacier showing rectilinear "lock-on" artifacts. Note that the dimensions of these artifacts correspond closely to speckle tracking chip size (64×192 pixels in range and azimuth respectively).

a SAR image.

To reduce the prevalence of false matches caused by multiplication of high intensity pixels, we propose a non-linear intensity rescaling that will be applied to SAR images before speckle tracking to reduce the impact of high intensity pixels on the NCC.

Creating a simulated SAR image pair

To confirm that intensity rescaling can improve SAR speckle tracking performance, and to identify a rescaling that performs well, we develop a SAR simulator capable of producing a realistic glacier speckle tracking pair with a known motion field. We identify three key requirements for a realistic SLC pair: 1) a partially correlated speckle pattern, 2) a glaciologically realistic motion field and 3) realistic terrain (e.g., supraglacial streams, moraines, etc.) and speckle patterns. To generate a realistic SLC pair, we start with a real SAR image, covering a glacierized area, as the initial scene in the speckle tracking pair. For the second image, we use an SLC formed from a combination of speckle patterns, terrain maps and motion fields extracted from actual SAR images of the same glacierized area (see Fig. 3).

The process begins by selecting an area of interest (see Fig. 1) on Thompson Glacier that contains both

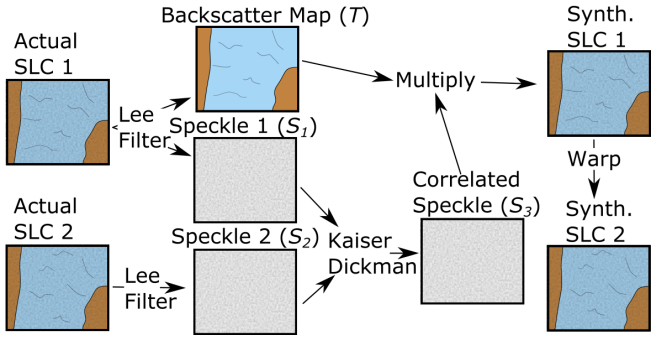

Fig. 3. Schematic outlining the process for generating the second synthetic SAR image used in the simulated SAR speckle tracking pair. Actual SLC 1 and synthetic SLC 2 will be used as the image pair.

the glacier margin, meaning that a significant velocity gradient will be captured, along with a large and perennial supraglacial channel across which discontinuous glacier motion is suspected to occur. Both the glacier margin and the channel provide clusters of high intensity pixels that may result in false speckle tracking matches.

After selecting the area of interest, two (globally coregistered) SLCs are cropped to contain this common area. The two images are chosen to maximize the temporal separation, and thus glacier surface change, which results in the speckle patterns between them being as decorrelated as possible. The selected images were acquired on 15 February 2018 and 22 May 2018, comprising the first and last SLCs available with matching acquisition parameters. The SLC collected on 15 February 2018 will serve as the initial image in the simulated speckle tracking scene pair.

A Lee filter (Lee, 1983) with a 3×3 pixel windows is used to obtain both the terrain backscatter map, T (i.e., a speckle free image) and the speckle pattern S_1 from the initial real SLC. A 3×3 pixel window is chosen in order to minimize blurring of surface features in the terrain map. The same Lee filter is also used to obtain S_2, the speckle pattern from the second real SLC. The major benefit of obtaining these speckle patterns from real data is that glacier features such as marginal moraines will be captured in S_1 and S_2 if these features happen to exhibit some control on the speckle patterns.

To form the second, simulated SLC in the speckle tracking pair, a speckle pattern that is partially correlated with S_1 is necessary. This partial correlation simulates the minor changes in the glacier surface that are inevitable over the 24-day repeat period of RADARSAT-2. S_3, the speckle pattern for the second simulated SLC, is formed by combining S_1 and S_2 using the Kaiser-Dickman algorithm (Kaiser and

Dickman, 1962):

$$S_3 = \rho\, S_1 + \sqrt{\rho - 1}\, S_2, \tag{2}$$

where ρ is the desired coherence. For our experiments, we chose $\rho = 0.8$, which results in a mean NCC of 0.543 for the simulated scene pair. This value is comparable to the mean NCC, for the same geographic area, of the most coherent scene pairs used in this study and represents a realistic but favorable scenario (i.e., little glacier surface change). To obtain the second SLC for the speckle tracking pair, S_3 is normalized to unit mean to ensure it does not change the overall intensity of the second synthetic SLC and is then multiplied element-wise by the terrain backscatter intensity map T (Xie and others, 2002).

A realistic glacier motion field is then introduced to the second simulated SLC using Lanzos resampling and a user-defined lookup table. The realistic glacier motion field itself is generated by taking the speckle tracking results from the 15 February 2018 and 11 March 2018 SLCs and smoothing the resulting motion field using a 20×60 pixel (approximately 30×30 m) boxcar filter.

Optimal intensity transformation

We begin by using the SAR simulator described above to test intensity transformations that follow

$$I_t = I^{(1/k)} \mid k \in \{1, 1.5, 2, 2.5, 3, 3.5\}, \tag{3}$$

where I represents the normalized intensities, achieved by dividing the original image by the mean intensity of the SLC. $k = 1.5$ gives the best performing intensity transformation on the basis of mean absolute error (MAE) between the speckle tracking results and the imposed motion field. However, despite the measured MAE improvement, the speckle tracking results still pronounce outlier-type errors, appearing as rectilinear artifacts (e.g., Fig. 2), around the bright pixels that form the supraglacial channel in the simulated image pair. Thus, we test a piecewise transformation that applies a higher value of k, denoted k_h, to pixels above some intensity threshold. The piecewise transformation is given by

$$I_t = \begin{cases} I^{1/1.5} & I < t \\ I^{1/k_h} + (t^{1/1.5} - t^{1/k_h}) & I \geqslant t, \end{cases} \tag{4}$$

where t is a threshold intensity and the term $(t^{1/1.5} - t^{1/k_h})$ ensures that the piecewise function is continuous and monotonically increasing. A grid search with $k_h \in \{2, 3, 4, 5\}$ and $t \in \{1, 1.5, 2, 2.5, 3\}$ shows

that $k_h = 3$, $t = 2$ yields the best performance with a MAE of 0.0477. This transformation represents a 23% improvement over the untransformed case for the simulated speckle tracking pair.

Speckle tracking methods

To measure glacier motion, intensity-transformed speckle tracking is performed at the full image resolution (i.e., a one pixel step in both range and azimuth) using an upsampling factor of two and a 64×192 pixel correlation chip (prior to upsampling) in range and azimuth respectively. The chip size, which corresponds to a ground footprint of approximately 80×80 m, is intended to be small enough to capture the glacier motion of interest while still being large enough to provide robust matches. The upsampling factor is chosen as a compromise between accuracy and computational cost (Magnard and others, 2017). A minimum cross correlation threshold of 0.1 is used, where matches that fall below this threshold are discarded. The speckle tracking itself is carried out using the GAMMA software's `offset_pwr_tracking` function.

Speckle tracking is only capable of measuring the glacier motion field in a 2-D plane defined by the range and azimuth directions. To convert the measurements in this plane into glacier motion, we use the surface-parallel flow assumption (e.g., Cumming and Zhang, 1999; Joughin and others, 2018) which assumes that the true motion vector lies in the plane that is locally tangent to the glacier surface, equivalent to assuming that emergence/submergence velocities are negligible over the temporal baseline of the speckle tracking pair. In select cases, two speckle tracking results from substantially different look geometries overlap in time and space, allowing for inversion of the full 3-D velocity field (e.g., Wang and others, 2019). ArcticDEM 7 (Porter and others, 2018) is used to define the locally tangent glacier surface necessary for the surface-parallel assumption and for the geocoding used to align the two speckle results employed in the 3-D velocity inversion.

For scenes of interest that contain the Astro Channel, where speckle tracking results indicate a substantial cross-channel velocity discontinuity, masked speckle tracking is carried out. Here, ice on each side of the channel is tracked separately (i.e., the other side is masked out) to ensure that speckle tracking chips do not straddle the channel itself.

REMOTE SENSING RESULTS AND DISCUSSION

Intensity transformed speckle tracking is used to track glacier motion for the 30 scene pairs (see Table S1) collected over the Expedition Fjord Area. In all cases, the scene pairs are formed from SLCs collected 24

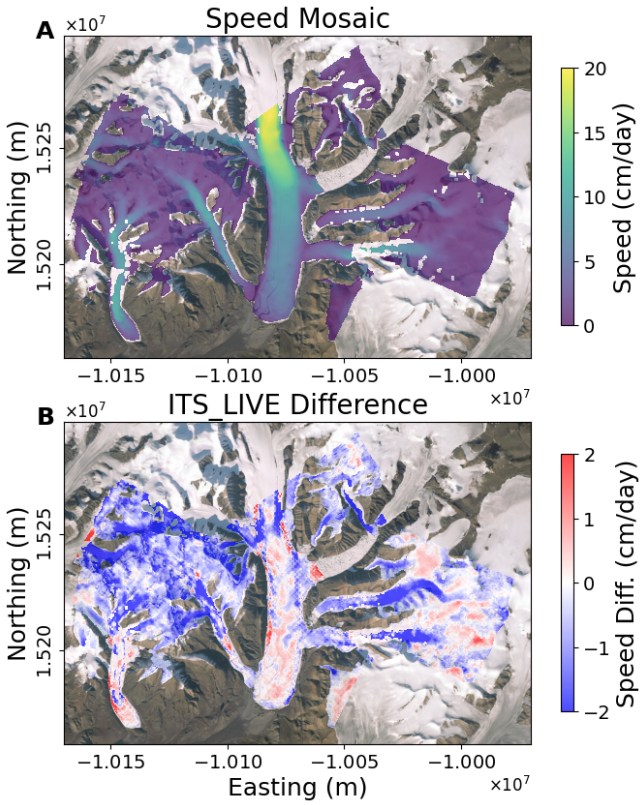

Fig. 4. Surface flow speed from SAR speckle tracking versus NASA ITS_LIVE data. (a) Average glacier speed as measured by speckle tracking under the surface parallel flow assumption and (b) Difference (ITS_LIVE-SAR) between NASA ITS_LIVE data and speckle tracking results. Note that the ITS_LIVE data are annual velocities whereas the speckle tracking data cover only winter and spring. ITS_LIVE velocity data are generated using auto-RIFT (Gardner and others, 2018) and provided by the NASA MEaSUREs ITS_LIVE project (Gardner and others, 2022). Optical imagery courtesy of Esri World Imagery (Esri, 2022).

days apart. Glacier speeds resulting from speckle tracking under the surface-parallel flow assumption (Fig. 4) match velocity data from NASA ITS_LIVE closely, with a mean absolute error of $0.88\,\mathrm{cm\,d^{-1}}$.

Broken fringes

The glacier motion maps produced by SAR speckle tracking, along with ArcticDEM (Porter and others, 2018), are also used for InSAR analysis. We create interferograms sensitive only to glacier motion along the satellite line-of-sight which show broken fringes in three different areas of Thompson Glacier. In all three cases, the broken fringes align with large, persistent supraglacial channels that are visible in optical satellite imagery dating back until at least 2009 and appearing in the same location in all RADARSAT-2 scenes used in this study which date from 2012, 2013, 2014, 2015, 2018 and 2022. Each channel appears

to be fed by an ice-marginal lake. We refer to these three channels as the Upper Channel, West Channel and Astro Channel (see Fig. 1).

Broken InSAR fringes can be the result of 1) discontinuous motion, 2) a topographic discontinuity (i.e., a cliff or other steep topographic feature) that is not present in the DEM or 3) a topographic discontinuity present in the DEM but that did not exist when the SAR data were collected. Mechanism 3 is easily ruled out by examining the DEM, which contains no steep gradients in the areas of the broken fringes. Mechanism 2 can be investigated as fringe spacing resulting from topography would exhibit an inversely-proportional stereo-like sensitivity to the spatial baseline (i.e., a measurement of the distance between the two acquisition positions of the SAR satellite) of the scene pairs while fringes from motion fields would remain constant as the spatial baseline changes (Pepe and Calò, 2017). Examination of consecutive interferograms with the same acquisition parameters (e.g., Figs. 5, S1, S2), with baselines that vary by up to a factor of 4, show highly consistent fringe patterns, indicating that the broken fringes result from persistent discontinuous glacier motion.

3-D velocity profiles

To better characterize and visualize the Astro Channel discontinuity, we plot velocity profiles by sampling 3-D velocity rasters across transects that run perpendicular to the channel. For each profile, velocities are plotted from both the masked and unmasked 3-D inversion rasters. Fig. 6 shows these profiles for the 3-D inversion results from the 29 January 2022 and 22 February 2022 (ascending) and 25 January 2022 and 18 February 2022 (descending) scene pairs which have the highest coherence of all the 3-D velocity inversions. These velocity profiles show that while the magnitude of the velocity discontinuity varies from location to location, the central (western) ice moves approximately $1\,\mathrm{cm\,d^{-1}}$ faster than the marginal (eastern) ice. Velocity profiles are also plotted across the Upper and West channels (See Figs. S4 and S3) but no discontinuous motion is visible in the resulting profiles, indicating that the discontinuous motion is too small ($\lesssim 0.5\,\mathrm{cm\,d^{-1}}$) to be resolved by speckle tracking.

As these profiles are sampled from the 3-D velocity rasters, it is also possible to separate the Easting, Northing, Up (ENU) direction components of the discontinuous motion (Fig. 6f–i). Doing so shows that the discontinuity is mainly (>75 % in profiles 1 and 2) the result of differences in the north/south velocity component, which is approximately aligned with the direction of the Astro Channel. This is noteworthy as it means that the discontinuous motion along the Astro Channel is largely the result of differences in

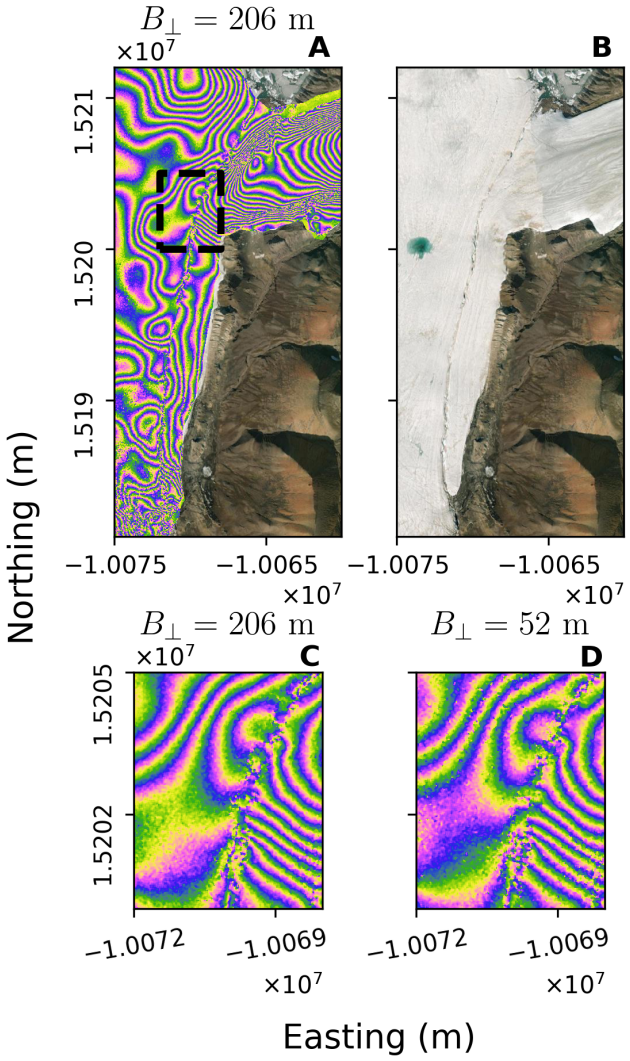

Fig. 5. Broken SAR interferometric fringes across the Astro Channel along with optical imagery. The interferogram in (a) and (c) is created using data from 15 February 2018 and 11 March 2018. The interferogram in (d) is created using data from 11 March 2018 and 4 April 2018. Panels (c–d) show a closeup of the respective interferogram in the area around the channel. Note that despite the significant difference in $B_\perp$, the magnitude of the fringe discontinuities is approximately equal in both interferograms, indicating discontinuous motion as opposed to discontinuous topography. Optical imagery courtesy of Esri World Imagery (Esri, 2022).

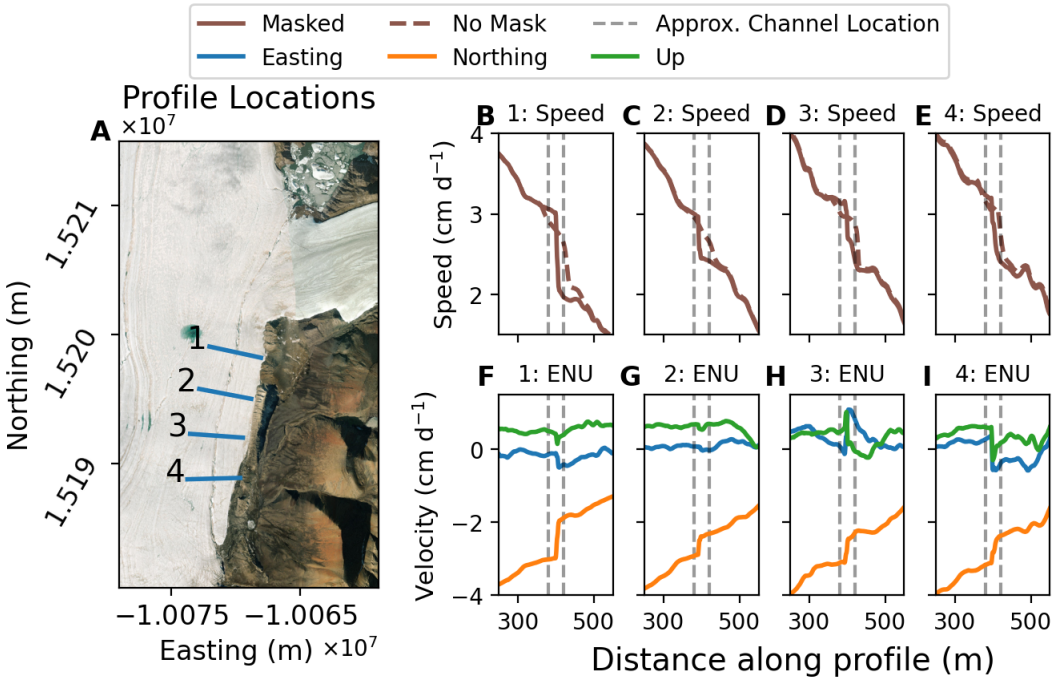

Fig. 6. 1-D profiles from 3-D inversion results from the 29 January 2022 and 22 February 2022 (ascending) and 25 January 2022 and 18 February 2022 (descending) scene pairs. The location and number of each profile are shown in (a) and the speed along the profile is shown in (b–e). Results for both the masked and non-masked SAR speckle tracking are shown as the dashed and solid brown lines respectively. The profile velocity results, separated into ENU components are shown in (f–i). Note that the negative sign of the y-axis scale is the result of the ice largely moving south. The dashed black lines in (b–i) indicate the approximate location of the channel as obtained from manual delineation of the channel in optical satellite imagery. Optical imagery courtesy of Esri World Imagery (Esri, 2022).

ice velocity in the along-channel direction as opposed to differences in vertical velocities or some form of overriding behavior similar, for example, to that observed at the confluence of Berendon Glacier (Eyles and Rogerson, 1977).

Temporal limitations

The speckle tracking pairs used in this study are derived from SAR images collected during only winter and spring in order to limit the temporal decorrelation caused by surface melt, and thus maximize the accuracy of speckle tracking and InSAR. However, Thompson Glacier, like many polythermal glaciers, likely exhibits seasonal velocity fluctuations (Thomson and Copland, 2017; Rabus and Echelmeyer, 1997) characterized by increased velocities during the short melt season. No summer velocity measurements exist for Thompson Glacier, but the neighboring White Glacier, which has velocity records dating back to the

1970s, shows summer velocity increases up to approximately 50% over winter velocities along a profile near the glacier terminus (Thomson and Copland, 2017). On White Glacier, both the absolute and relative magnitude of these summer velocity increases are greatest at a profile near the terminus and lower at an upglacier profile. These summer velocity increases are likely caused by high basal water pressure which leads to reduced friction at the glacier bed (Bingham and others, 2006; Thomson and Copland, 2017).

If a similar seasonal cycle occurs on Thompson Glacier, then the speckle tracking results presented here do not capture this seasonal period of elevated glacier velocities. Thus the velocity maps presented in this study should represent a slight underestimate of the annual glacier velocities, with the underestimate likely being greatest near the glacier termini. Indeed, this may partially explain the spatial structure seen in Fig. 4b where the annual velocities from NASA ITS_LIVE data are generally greater than the SAR derived velocities near the terminus. However, it should also be noted that the SAR speed mosaic (Fig. 4a) does not account for emergence velocities and is largely derived from different time periods than the ITS_LIVE data which, alternatively, may explain why the SAR-derived velocities are higher than the ITS_LIVE velocities in some areas.

ICE-FLOW MODELING METHODS

We employ a two-dimensional cross-sectional ice-flow model in order to gain insight into possible causes of the discontinuous glacier motion observed at the supraglacial stream channel originating from Astro Lake (referred to as "the Astro Channel"). Specifically, the flow model is used to investigate the effects of channel depth, sliding behavior and glacier thermal structure on the magnitude of a velocity discontinuity across a cleft in a synthetic model domain inspired by the area of Thompson Glacier where the Astro discontinuity is observed. It should be emphasized that this model is not intended to simulate Thompson Glacier itself, as key information such as the bed profile, glacier thermal structure and even stream channel depth are either unknown or poorly constrained. Instead, this model is intended to 1) investigate whether a continuum (i.e., no ice fracture) model of glacier flow can produce velocity discontinuities comparable to those observed and, if so, 2) quantify the effects of glacier and stream channel thermal structure, channel depth and sliding behavior on the velocity discontinuity.

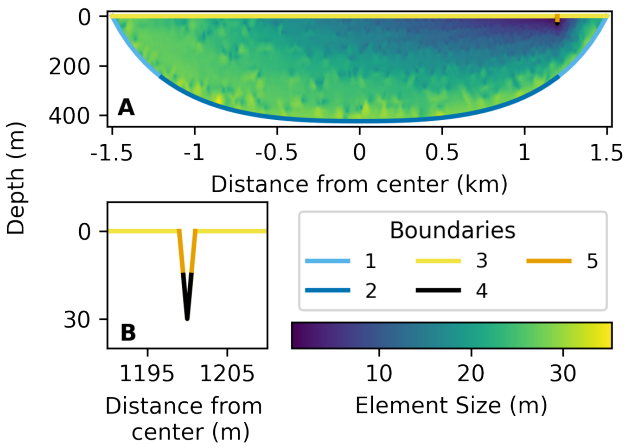

Fig. 7. The model domain for a channel depth of 30 m and a thermal transition location (L_t) 1200 m from center. (a) Model boundaries and element size, defined as the diameter of the circle that circumscribes the triangular element. 1.5 times vertical exaggeration. (b) Close up of the supraglacial stream boundaries. For the polythermal ice-flow models, boundary 1 is frozen to the bed, boundary 2 is either frozen to the bed or sliding according to a sliding-law coefficient and boundaries 3–5 are stress free. For the corresponding thermal models, a geothermal heat flux is applied along boundary 1, boundaries 2 and 5 have a heat flux of zero and boundaries 3 and 4 have a prescribed temperature based on plausible climatic conditions. These boundary conditions are described in greater detail in Table 1.

Model domain

The model domain (Fig. 7) represents a transverse cross section of a glacier that is 3 km wide and 425 m deep at the center with a stream channel of some depth incised into the glacier surface 300 m from the eastern margin. As the depth of the Astro Channel is uncertain, we use a number of different model domains with varying stream channel depths. The bed profile is created by selecting several control points that are then used to define a symmetrical basis spline curve that forms the bed profile. These control points, which consist of a depth and lateral position, are selected based on averages of the global ice thickness estimates (Farinotti and others, 2019; Millan and others, 2022) in the study area. The glacier surface slope θ is approximated as 2.15° based on ArcticDEM (Porter and others, 2018). Each channel depth yields a slightly different model domain. All domains use second-order triangular Lagrange elements on a nonuniform grid and have >15,900 individual elements. Mesh refinement tests show that the solutions converge with the chosen mesh resolution to the same values as finer-mesh tests. The mesh itself is generated using the open-source mesh generator `gmsh` (Geuzaine and Remacle, 2009).

This model domain, and the associated boundaries in Fig. 7, are used to separately model both glacier

thermal structure and ice flow. As no bed measurements exist for Thompson Glacier, we sometimes allow a possible basal thermal transition to occur between boundary 1 (frozen) and boundary 2 (temperate). The position of this boundary is permitted to vary within a 200 m horizontal range and a Weertman-type sliding law (Weertman, 1957) is introduced along boundary 2. In other cases, both boundaries 1 and 2 are frozen to the bed and no sliding occurs.

Ice-flow equations

We employ a steady state cross-sectional ice-flow model similar to those of Amundson and others (2006), Wilson and others (2013) and Armstrong and others (2016) in that our model captures lateral velocity gradients, is appropriate for the geometry of the study area and is computationally efficient enough to test a large set of model parameters. Following Nye (1965), we assume no compression or extension in the flow direction and no vertical or transverse flow, thus reducing the ice-flow equation to the nonlinear Poisson equation

$$\frac{\partial}{\partial z}\left(\eta\frac{\partial u}{\partial z}\right)+\frac{\partial}{\partial y}\left(\eta\frac{\partial u}{\partial y}\right)=-\rho g\sin\theta. \tag{5}$$

Here, y and z are the transverse and vertical coordinates respectively, u is the velocity, ρ is the ice density, g is the acceleration due to gravity, θ is the ice-surface slope and η is the stress-dependent ice viscosity:

$$\eta=\frac{1}{2}A^{-1/n}\dot{\varepsilon}_e^{-1+1/n}, \tag{6}$$

where A is the ice-creep parameter, $n=3$ and the effective strain rate is written

$$\dot{\varepsilon}_e=\frac{1}{2}\sqrt{\left(\frac{\partial u}{\partial z}\right)^2+\left(\frac{\partial u}{\partial y}\right)^2}. \tag{7}$$

In some model configurations we use a Weertman-type sliding law (Weertman, 1957; Minchew and others, 2016), defined as

$$\tau_b=Cu_b^{1/2}, \tag{8}$$

where τ_b is the basal shear stress, u_b is the basal velocity and C is the sliding-law coefficient, a constant related to basal friction. In all cases considered here, at least some portion of the bed is assumed frozen, along which a no-slip ($u_b=0$) Dirichlet boundary condition is imposed. In the sliding case $u_b=0$ is applied over boundary 1 and in the non-sliding case $u_b=0$ is applied over boundaries 1 and 2. A no-stress

Neumann boundary condition ($\nabla u = 0$) is prescribed along the glacier surface (boundaries 3, 4 and 5).

The above equations are solved using `Firedrake`, an open source, finite-element package designed to solve partial differential equations (Rathgeber and others, 2016; Shapero and others, 2021). As the ice viscosity η is non-linearly dependent on the velocity field u, and the sliding law requires a Neumann boundary condition that is dependent on $\sqrt{u}$, an iterative method is used to solve for u. We use Picard iteration, in which an initial guess for u is supplied in order to calculate η, which is then used to calculate a new value of u. This process is repeated until the change in u between consecutive iterations is sufficiently small. For the purpose of Picard iteration, the difference between two consecutive velocity field solutions, u_k and u_{k+1}, is defined as the element-wise maximum absolute difference between u_k and u_{k+1}. For all model runs presented here, this difference threshold is set as 0.04 mm/day (1 mm/24 days), which is approximately 1/1000 of the central velocity of Thompson Glacier in the vicinity of the Astro Channel.

Thermal structure

Glacier thermal structures are generated by using `Firedrake` to solve a steady state heat diffusion equation under a variety of boundary conditions with internal heat sources. It should be stressed that this method is not intended to simulate the thermodynamic processes occurring in glaciers but rather to flexibly produce a variety of plausible glacier thermal structures that can be used to define the scalar field A (6). The diffusion equation is given by

$$\int_{\Omega} [k(T) \cdot \nabla(T) \cdot \nabla(w) - f_1(y)\, w]\, dx = 0, \tag{9}$$

where $k(T)$ is the thermal conductivity of ice, T is the temperature field and trial function, w is the test function, $f_1(y)$ is a piecewise, spatially varying heat flux, and Ω is the model domain (see supplementary materials for more details). The piecewise heat flux serves to slightly alter the thermal structure of the ice east of the channel, corresponding, in the real world, to the ice originating from Piper Glacier.

Along the upper surface of the glacier (boundary 3) and the bottom half of the channel (boundary 4), Dirichlet boundary conditions are applied where $T = T_s$ and $T = T_c$, respectively (see Table 1). Along the frozen bed margins (boundary 1), a heat flux of 40 mW m^{-2} is applied based on values reported at the toe of White Glacier (Blatter, 1987) and geothermal heat flux maps of the Canadian Arctic Basin (`https://www.cangea.ca/nunavutgeothermal.html`). Along the central bed (boundary 2), a temperature of either $T = -0.5$°C is prescribed in models with no sliding or the temperature is set to the pressure melting

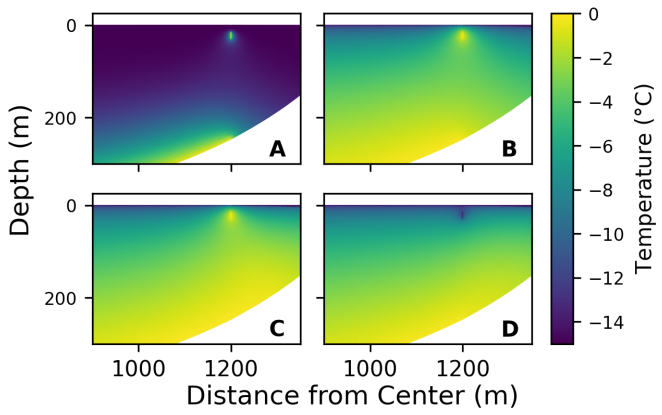

Fig. 8. Examples of generated thermal structures. Panel a) has $D_c = 30\,\mathrm{m}$, $T_s = -15^{\circ}\mathrm{C}$, $T_c = 0^{\circ}\mathrm{C}$, F_t=0 $\mathrm{mW\,m^{-2}}$, $G_t = 3$, $C = 1 \times 10^8\,\mathrm{Pa\ m\,s^{-1}}$ with each subsequent panel being identical to the previous except for one changed parameter. These changes are b) $G_t = 1/3$ c) F_t=2/1500 $\mathrm{mW\,m^{-2}}$ d) $T_c = -15^{\circ}\mathrm{C}$.

point (PMP) of pure ice if sliding is to occur. This PMP is calculated using only the ice overburden pressure, as the model assumes no compression or extension along the flowline. Finally, to prevent numerical instabilities that occur in the presence of steep temperature gradients due to low surface temperatures (boundary 3) and high channel temperatures (boundaries 4 and 5), a no-heat-flux boundary condition is prescribed over boundary 5.

Solving the heat equation under the conditions outlined above yields a uniform vertical temperature gradient in ice unaffected by the tributary (f_1) and geothermal (boundary 1) heat fluxes. In order to generate variable vertical temperature gradients, as are usually observed in glaciers, a non-linear rescaling is applied to the temperature fields after their initial generation. This rescaling preserves the minimum and maximum temperature values and is given by

$$T = (T_{\max} - T_{\min}) \times \left(\frac{T - T_{\min}}{T_{\max} - T_{\min}} \right)^{G_t} + T_{\min}, \tag{10}$$

where T is temperature, $T_{\max}$ ($T_{\min}$) is the maximum (minimum) value in the temperature field and G_t is the temperature gradient factor. Ice temperatures exceeding the PMP are clipped at this value.

The resulting temperature fields (see Fig. 8 for examples) are then converted into ice viscosity values for use in the ice-flow model. According to Cuffey and Paterson (2010), the relationship between the ice temperature T (°C) and A is given by

$$A = A_* \exp\left(-\frac{Q_c}{R} \left[\frac{1}{T_h} - \frac{1}{T_*} \right] \right), \tag{11}$$

where $A_* = 3.5 \times 10^{-25}$ Pa^{-3} s^{-1} is the value of A at -10°C, $T_* = 263 + 7 \times 10^{-8} P$, $T_h = T + 7 \times 10^{-8} P$, P is the pressure and

$$Q_c = \begin{cases} Q^- = 6 \times 10^4 \text{ J mol}^{-1} & T_h < T_* \\ Q^+ = 11.5 \times 10^4 \text{ J mol}^{-1} & T_h > T_*. \end{cases} \tag{12}$$

As (5) assumes no compression or extension in the x or y directions (Nye, 1965) we set $P = -z\,\rho\,g$, the ice overburden pressure where $-z$ is the depth within the glacier and $\rho = 917\,\text{kg m}^{-3}$, the density of pure ice.

Model parameters

We aim to select a set of model parameters that result in thermal structures, channel depths and sliding behaviors that cover the range of plausible scenarios for Thompson Glacier. In some cases, model parameters that fall outside the plausible range for Thompson Glacier are selected as they may provide insight into the general phenomenon of discontinuous motion across a channel. The selected set of model parameters are reviewed below and summarized in Table 1. Note that all selected parameter combinations were tested and included in the model analysis except for those that exhibit numerical instabilities.

The selected glacier surface temperatures (T_s) range from -10°C to -20°C, a range based on mean annual air temperatures in the Canadian High Arctic and in the vicinity of the study area. Channel temperatures (T_c) range between the glacier surface temperature and 0°C, which represents water flowing in the channel. Additionally, to represent the possibility of cold-air pooling in the channel, a value of T_c 2 K below T_s is tested. Modeled channel depths extend to 30 m, which is the maximum supported by field observations (Maag, 1963). Small heat fluxes (F_t), resulting in a temperature variation of ± 2 K, are prescribed in the ice east of the channel, corresponding, in the real-world, to ice originating from Piper Glacier. Non-physical temperature gradient factors (G_t) are introduced to mimic non-linear temperature-depth gradients as are found in many glaciers. We test factors that give both concave up and concave down temperature-depth profiles. Values of C, which describe the basal friction, are selected to give a wide range of sliding ratios while resulting in realistic sliding speeds. A zero sliding case is also included in our tests. Finally, the thermal transition location (L_t), in other words, the lateral position of the basal slip-to-no-slip transition that occurs at the intersection of the frozen margin and the thawed bed, is allowed to vary from the lateral position of the channel by up to ± 100 m in each direction. Further justification for the model

Symbol	Description	Location	Values	Units
T_s	Temperature	Glacier surface	[−10,−12.5,−15,−17.5,−20]	°C
T_c	Temperature	Channel	[0, −5, −10, $T_s - 2$, T_s]	°C
D_c	Channel depth	Channel	[10, 12.5 15, 17.5, 20, 22.5 27.5, 30]	m
F_t	Heat flux	Tributary ice	[−2/1550,−1/1550, 0, 1/1550, 2/1550]	mW m^{-2}
G_t	Temperature gradient factor	Everywhere	[1/3, 1/2, 1, 2, 3]	1
C	Sliding-law coefficient	Central bed	[1×10^8, 3.5×10^8, 7×10^8, None]	Pa m s^{-1}
L_t	Thermal transition location	Frozen margin	[1100, 1150, 1200, 1250, 1300]	m

Table 1. Parameters used to generate glacier thermal structure, model domain and sliding behaviour. Note that channel depth (D_c) is the only parameter that alters the model domain and that the values used to describe L_t correspond to the coordinate system shown in Fig. 7.

parameter selections are given in the supplementary material.

Temperate glaciers

As a point of comparison, we model a set of temperate glaciers with varying channel depths and sliding behaviors. For these temperate glaciers, the same bed profile is used and the ice temperature is chosen to be at the PMP everywhere. A Dirichlet boundary condition of $u_b = 0$ is prescribed along a 1 m swath of the bed at the outermost edges of the glacier domain. This is done as, for (5), a Dirichlet boundary condition must be prescribed somewhere or the velocity field can only be determined up to a constant. Note that this will not alter the metrics we use to measure the discontinuity as both are unaffected by any constant velocity offset. We model two end-member types of sliding behavior: a high slip case ($C = 1.0 \times 10^8$ Pa m s^{-1}) and a no-slip case ($u_b = 0$ for the entire bed). Sliding is calculated using the same Weertman-type sliding (8) law employed in the polythermal glacier modeling. The no-sliding case is not physically realistic for temperate glaciers but does provide a useful lower bound for low slip beds.

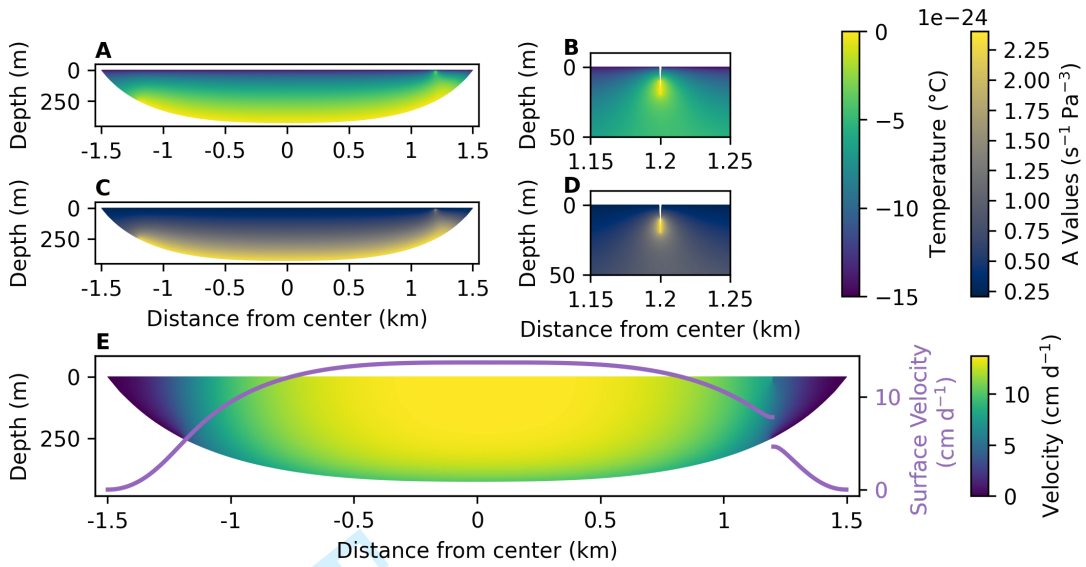

Fig. 9. Model results for $T_s = -15°C$, $T_c = 0°C$, $D_c = 20\,m$, $F_t = 2/1550\,mW\,m^{-2}$, $G_t = 1/2$, $C = 3 \times 10^8\,Pa\,m\,s^{-1}$ (see Table 1). (a) Temperature. (b) Close-up of (a). (c) Flow-law coefficient A. (d) Close-up of (c). (e) Velocity field and surface velocity.

ICE-FLOW MODELING RESULTS AND DISCUSSION

Polythermal glaciers

We model 134,758 numerically stable simulations with unique combinations of glacier thermal structures, channel depths and sliding behaviors. Fig. 9 shows examples of spatially distributed model outputs, including glacier temperatures, the corresponding values of A and glacier velocities. For each model run, the surface velocity on either side of the channel, the central surface velocity and central basal velocity are output. A non-dimensional discontinuity fraction, defined as the magnitude of the discontinuity divided by the velocity range of the glacier, is computed as a metric of discontinuity size relative to the overall glacier velocity (Fig. 10h–j).

The velocity range, as opposed to the velocity maximum, is used in calculating the discontinuity fraction as it removes any component of plug flow, thus allowing a direct comparison between polythermal and temperate glacier simulations. For the polythermal glaciers discussed here, the velocity range is equivalent to the maximum velocity and using the velocity range has no effect on the discontinuity fraction.

The modeled glaciers produce discontinuity fractions ranging from 0.040 to 0.370 with a mean of 0.137 (Fig. 10). For reference, the observed discontinuity fraction across Astro Channel is approximately 0.13. These fairly substantial discontinuity fractions are, themselves, a key result. They demonstrate that it is

possible to achieve non-negligible discontinuous surface velocity fields such as those observed across the Astro Channel in the absence of ice fracture or highly specific thermal structures or sliding behaviors. The occurrence of cross-channel velocity discontinuities in the absence of ice fracture is in line with other work (e.g., Moore and others, 2010; Monz and others, 2022) that casts doubt on ice fracture being responsible for structures attributed to thrust faulting. Indeed, the modeling shows that a fairly wide range of thermal structures and channel depths should give rise to discontinuous velocity fields detectable by high resolution remote sensing.

Several factors related to the discontinuity fraction distributions shown in Fig. 10a–g should be noted. First, channel depth is the only single variable that has a strong control on both the minimum and maximum discontinuity fraction. With all other variables, the maximum discontinuity fraction may change with variable choice but the minimum discontinuity fraction remains close to zero. This change in maxima only is most pronounced for the channel temperature, in which cold channels limit the maximum discontinuity fraction more strongly than their warm counterparts. A similar, albeit weaker, phenomenon occurs with the bed friction parameter C, surface temperature and temperature gradient factor.

Temperate glaciers

We model temperate glaciers with channel depths of D_c (see Table 1). For each channel depth, the temperate discontinuity fractions (see Fig. 10a) closely bound ($\leqslant \pm 16\%$) the smallest polythermal fractions for corresponding channel depths, while the temperate magnitudes (See Fig. S5) exceed the median of their polythermal counterparts by at least 20%. However, the smaller temperate discontinuity fractions are due to the comparatively large surface velocities of the temperate glaciers, as opposed to small cross-channel velocity discontinuities.

Model limitations

The cross-sectional nature of the ice-flow model discussed above results in several shortcomings, notably it neglects the longitudinal compression that results in measurable emergence velocities and inherently assumes that the glacier geometry (including the supraglacial channel) and thermal structure are longitudinally uniform. These geometric assumptions imply that the modeled supraglacial channel is infinitely long and perfectly straight, resulting in a discontinuity maximizing scenario as compared to channels that exhibit overall curvature or sinuosity. While channel curvature or sinuosity should reduce the discontinuity

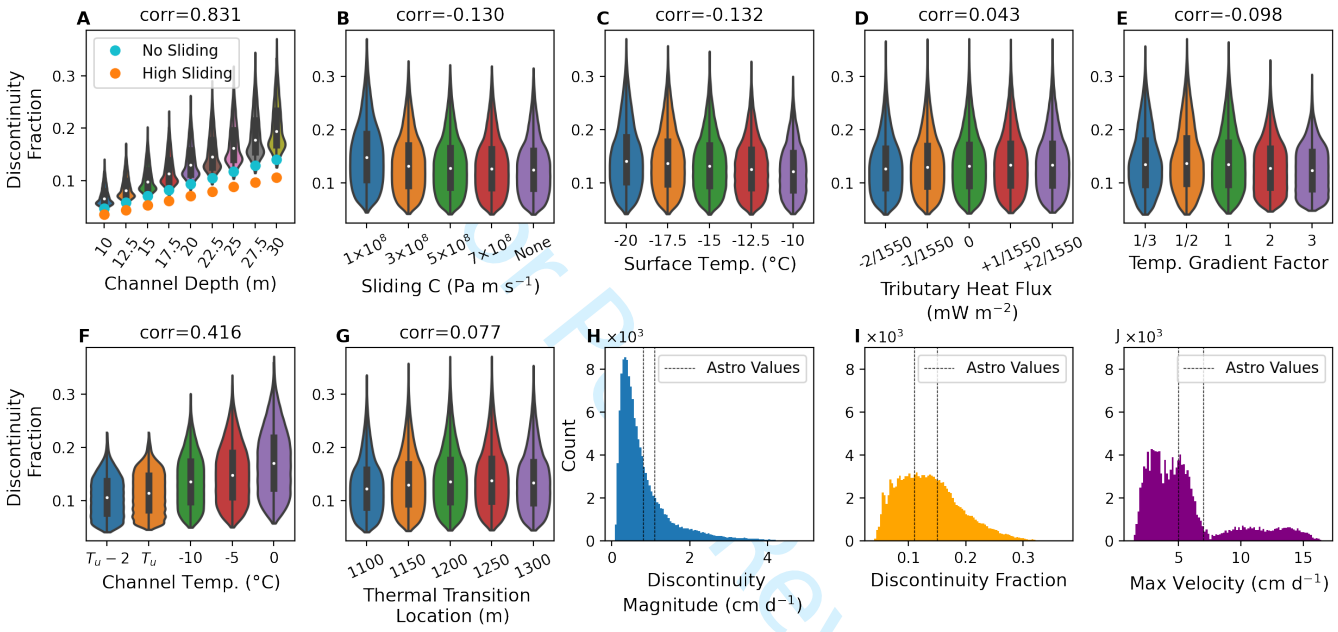

Fig. 10. Violin plots (a–g) for each model parameter in Table 1 and histograms (h–j) for all model results. Violin plots include Spearman correlation scores for discontinuity fraction and parameter along with a box plot showing the mean (white dot) and inter-quartile range (thick black bar). Panel (a) includes discontinuity fraction for the temperate glaciers with varying channel depths and sliding behaviors (orange and blue dots). For the high sliding case $C = 1.0 \times 10^8$ Pa m s^{-1}. Dashed black lines in (h–j) indicate the approximate range of values observed at the Astro discontinuity.

magnitude for a given set of model parameters, it is unclear how substantial the impact will be.

However, the largest shortcoming of the ice-flow model used above is not related to its cross-sectional nature but instead results from the lack of thermomechnical coupling. For the modeled glaciers, the thermal structure is simply generated by solving a heat diffusion equation over the model domain using boundary conditions that are loosely based on the climate of the study site. This method of generating thermal structures greatly reduces the complexity and computational cost of the model but fails to account for the thermal effects of ice advection and strain heating. A key result of the missing advection is that the temperature gradient with depth resulting from the heat diffusion equation is always linear and must be rescaled with a temperature gradient factor in order to achieve the depth-varying temperature gradients found in real glaciers. The lack of strain heating will impact the thermal structure, and thus the velocity field, throughout the glacier. At the discontinuity itself, where deformation rates are quite high, lack of strain heating and its ice softening effects may cause the model to underestimate the magnitude of the velocity discontinuity when compared to a thermomechanically coupled model.

While the lack of thermomechnical coupling yields less accurate glacier velocity fields, the simplicity and therefore low computational cost of the model allows for testing a large number of model configurations. The large parameter space explored is useful, as many important model parameters such as channel depth, surface temperature and channel temperature are either unknown or poorly constrained. Moreover, as the modeling is intended to give a general understanding of ice flow across large supraglacial stream channels, the additional accuracy gained from thermomechical coupling is not essential to the interpretation of model results.

DISCUSSION

Discontinuity causing channel geometry

The modeling results indicate that cross-channel velocity discontinuities substantial enough to be measured by high resolution remote sensing or in-situ methods can occur under a wide variety of thermal conditions (including in temperate glaciers) and sliding behaviors, and do not require implausibly deep supraglacial channels. However, observations of these cross-channel velocity discontinuities remain rare to date. The lack of observations likely occurs for two reasons. First, researchers are simply not measuring velocity fields across supraglacial channels using in-situ methods. In addition, remote sensing that happens to image areas in which cross-channel velocity discontinuities occur will likely be unable to resolve the discontinuities unless

a high resolution sensor is used. The sensor resolution necessary to detect a cross-channel discontinuity will depend on the temporal baseline and discontinuity magnitude, but a sensor capable of resolving glacier motion of $\sim 1\,\mathrm{cm\,d^{-1}}$ is a reasonable estimate. Furthermore, significant spatial smoothing, which is commonly performed on remotely sensed glacier velocity fields, will likely obscure any discontinuous motion.

Second, and more importantly, for supraglacial channels to form discontinuous motion fields, specific geometric requirements must be met. As the local transverse velocity gradient is proportional to the discontinuity fraction and magnitude (see Fig. S6), the channel must be positioned in a region of substantial lateral velocity gradients (and thus shear stresses) that are sustained over fairly long (likely kilometer-scale) distances. This means that the channel must be long and located in a band near the glacier margin where high shear stresses occur and run approximately parallel to the glacier flow direction. The channel must also be of substantial depth, $\gtrsim 10\,\mathrm{m}$ at a minimum. Supraglacial channels that meet these length and position criteria appear uncommon, but are more likely to occur on polythermal glaciers, which tend to have fewer drainage features such as moulins compared to their temperate counterparts (Bingham and others, 2003) and thus longer surpaglacial streams and channels.

Moreover, to form channels of sufficient depth, very high incision rates or perennial occupation by meltwater are necessary. On polythermal glaciers, perennial occupation by meltwater appears necessary as anomalously high incision rates compared to those that have been observed would be necessary to form channels of 10+ m depth in a single melt season (St Germain and Moorman, 2019; Irvine-Fynn and others, 2011). On temperate glaciers, where incision rates are generally higher than those found on polythermal glaciers, even when compared to the local ablation rates, it may be possible to form sufficiently deep channels in a single melt season with very high but still plausible incision rates (Isenko and others, 2005; Ferguson, 1973). However, some research indicates that the high discharge rates necessary to cut these channels in temperate glaciers are correlated with high sinuosity which would likely inhibit the velocity discontinuity by reducing the longitudinally averaged channel depth (St Germain and Moorman, 2019; Ferguson, 1973). Perennially occupied supraglacial channels, which may result in deep channels with lower sinuosity due to their lower discharge rates, are unlikely to form on temperate glaciers as high deformation rates would close the channel between melt seasons (Hambrey, 1977; Irvine-Fynn and others, 2011). Alternatively, if a velocity discontinuity across a sinuous supraglacial channel does occur, the differential motion may cause the channel to pinch itself shut as one bank of the channel migrates into the

other, provided the velocity discontinuity is greater than the rate at which the stream incises into the ice. In sum, the probability of a supraglacial channel meeting the length, depth and direction criteria necessary to cause a surface velocity discontinuity are small, with the most likely scenario occurring when perennial supraglacial streams form on polythermal glaciers.

Thompson Glacier channels

All three channels (i.e., Astro, West and Upper channels) on Thompson Glacier at which interferograms indicate the presence of discontinuous motion appear to match the length, depth and direction criteria to a degree. These three channels are large enough to appear prominently in satellite imagery, likely indicating that they are at least several meters deep although the Astro Channel appears wider, and thus probably deeper, than the Upper and West channels. All three channels are also approximately aligned with the direction of glacier flow for 2+ km. In the case of the Upper Channel, the distance from the glacier margin is approximately 400 m, similar to that of the Astro Channel, with the transverse velocity gradients, as measured by speckle tracking, being approximately twice as large as those in the vicinity of the Astro Channel. However, speckle tracking is unable to resolve a velocity discontinuity across the Upper Channel, indicating a cross-channel velocity difference of $\lesssim 0.5\,\mathrm{cm\,d^{-1}}$. This comparatively small velocity discontinuity, despite the larger transverse velocity gradient, is most easily explained as the result of a shallower channel depth. The West Channel is located approximately 900 m from the glacier margin, with transverse velocity gradients that are ∼10% of those at the Astro Channel. Again, speckle tracking is unable to resolve a velocity discontinuity across this channel, indicating a cross-channel velocity difference of $\lesssim 0.5\,\mathrm{cm\,d^{-1}}$. This comparatively small velocity discontinuity could result from a combination of low shear stresses across the West Channel, as indicated by the transverse velocity gradients, and shallower channel depths.

Controls on channel formation and geometry

The three supraglacial channels on Thompson Glacier where discontinuous motion is detected originate at glacier confluences and are fed by marginal lakes, likely indicating meltwater occupation for part of the year. We speculate that channels conducive to discontinuous glacier motion may form preferentially at glacier confluences due to structural controls imposed by the two flow units. From optical satellite imagery we discern, qualitatively, that many glaciers on Umingmat Nunaat (Axel Heiberg Island) have

long, flow-parallel supraglacial channels that originate at glacier confluences. Some, but not all, of these channels appear to be fed by ice-marginal lakes. Relatively little is known about what controls the location of supraglacial stream formation, however Hambrey (1977) has suggested that glacier structures, including flow units, may play some role in determining the location of small supraglacial streams. Moreover, Hambrey (1977) observed that many of these small streams follow structural features and, as a result, are often fairly straight. At a glacier confluence troughs may form between the two flow units (Glasser and Gudmundsson, 2012) which could create a structural feature that may potentially be exploited by water to form a long, flow-flowing supraglacial stream. Thus it is possible that larger flow units, such as glacier tributaries, may be able to control stream location and sinuosity leading to channels that are conducive to a discontinuous surface velocity field.

CONCLUSION

High resolution SAR speckle tracking of glaciers remains largely underleveraged but may be broadly useful to measure and investigate mesoscale (multi-centimeter) glacier motion. In this study, we use high resolution speckle tracking to investigate mesoscale discontinuous motion, initially detected by InSAR, across supraglacial stream channels on Thompson Glacier, Umingmat Nunaat (Axel Heiberg Island).

As the magnitude of the velocity discontinuities on Thompson Glacier are small (several $\mathrm{cm\,d^{-1}}$), spatial smoothing of the speckle tracking results, as is commonly done to reduce errors, obscures the discontinuities. Instead, we analyze the possible causes of speckle tracking errors and find that false matches often occur when speckle tracking locks-on to high intensity pixels, which in SAR images of glaciers, are often structural features such as crevasses or stream channels.

To improve SAR speckle tracking performance, we use a SAR simulator capable of generating SLC pairs with a user defined motion field to study optimum intensity rescaling as a pre-conditioning step. The intensity-rescaled speckle tracking is then used to measure the motion of the Expedition Fjord area glaciers. The measured glacier speeds compare well (MAE of $0.881\,\mathrm{cm\,d^{-1}}$) to annual speeds from NASA ITS_LIVE data, a lower resolution global glacier motion dataset. Interferograms indicate that cross-channel discontinuous motion is occurring along three supraglacial channels on Thompson Glacier. However, only at the Astro Channel is the magnitude of the velocity discontinuity large enough to be resolved by the speckle tracking results, indicating that the discontinuity at the other two channels is $\lesssim 0.5\,\mathrm{cm\,d^{-1}}$. The remote sensing observations show an uncommon form of discontinuous glacier motion characterized by ice on

the central (west) side of the Astro Channel flowing approximately 30% ($1\,\mathrm{cm\,d^{-1}}$) faster than the ice immediately across the $\sim$3 m wide channel.

A cross-sectional ice-flow model is used to investigate this discontinuous motion. The finite-element ice-flow model uses a domain inspired by Thompson Glacier that includes a surface channel similar to the Astro Channel. The modeling shows that discontinuous glacier motion of the form and magnitude observed across the Astro Channel can occur, without ice fracture and under a wide variety of plausible channel depths and thermal structures, including in temperate glaciers.

We also use the ice-flow model to investigate the sensitivity of the velocity discontinuity to various model parameters. Channel depth is the primary control on the velocity discontinuity, but low surface temperatures and high in-channel temperatures, caused in the real world by water flow within the channel, also contribute to larger cross-channel velocity discontinuities. Again, the modeling demonstrates that specific or unusual thermal structures are not necessary to cause cross-channel discontinuous motion, implying that the rarity of this form of motion is instead a result of the channel geometry. Namely, the channel must be deep (likely $\gtrsim$10 m), straight, flow-following and long, and located in areas of high lateral shear stress. We speculate that channels conducive to discontinuous motion form and persist preferentially on polythermal glaciers, particularly in the presence of glacier confluences and their associated ice-marginal lakes.

SUPPLEMENTARY MATERIAL

The supplementary material for this article can be found at https://doi.org/xxxxxx

ACKNOWLEDGEMENTS

SFU, NSERC, CSA and MDA contributed funding for this study. We thank MDA for their support in obtaining RADARSAT-2 data and acknowledge J Eppler for helpful discussions on creating simulated SAR images.

AUTHOR CONTRIBUTIONS

BR broadly conceived of the remote sensing portion of this study with specifics determined by GC. GC conceived of the glacier modeling portion with input from GF and BR. GC carried out both remote sensing

and ice-flow analysis and modeling with with guidance from BR and GF. GC led manuscript preparation with advice and editing from BR and GF.

REFERENCES

Amundson JM, Truffer M and Lüthi MP (2006) Time-dependent basal stress conditions beneath Black Rapids Glacier, Alaska, USA, inferred from measurements of ice deformation and surface motion. *Journal of Glaciology*, **52**(178), 347–357 (doi: 10.3189/172756506781828593)

Armstrong W, Anderson R, Allen J and Rajaram H (2016) Modeling the WorldView-derived seasonal velocity evolution of Kennicott Glacier, Alaska. *Journal of Glaciology*, **62**(234), 763–777 (doi: 10.1017/jog.2016.66)

Bamler R and Eineder M (2005) Accuracy of differential shift estimation by correlation and split-bandwidth interferometry for wideband and delta-k SAR systems. *IEEE Geoscience and Remote Sensing Letters*, **2**(2), 151–155 (doi: 10.1109/lgrs.2004.843203)

Bamler R, Eineder M, Adam N, Zhu X and Gernhardt S (2009) Interferometric potential of high resolution spaceborne SAR. *Photogrammetrie-Fernerkundung-Geoinformation*, **5**, 407–419 (doi: 10.1127/1432-8364/2009/0029)

Bingham RG, Nienow PW and Sharp M (2003) Intra-annual and intra-seasonal flow dynamics of a High Arctic polythermal valley glacier. *Annals of Glaciology*, **37**, 181–188 (doi: 10.3189/172756403781815762)

Bingham RG, Nienow PW, Sharp M and Copland L (2006) Hydrology and dynamics of a polythermal (mostly cold) High Arctic glacier. *Earth Surface Processes and Landforms: The Journal of the British Geomorphological Research Group*, **31**(12), 1463–1479 (doi: 10.1002/esp.1374)

Blatter H (1987) Stagnant ice at the bed of White Glacier, Axel Heiberg Island. N.W.T, Canada. *Annals of Glaciology*, **9**, 35–38 (doi: 10.1017/s0260305500000343)

Closson D and Milisavljevic N (2017) InSAR coherence and intensity changes detection. In *Mine Action - The Research Experience of the Royal Military Academy of Belgium*, InTech (doi: 10.5772/65779)

Cogley J and Adams WP (2000) Remote-sensing resources for monitoring glacier fluctuations on Axel Heiberg Island. *Arctic*, **53**(3), 248–259, ISSN 00040843 (doi: 10.14430/arctic856)

Cogley J, Adams WP and Ecclestone M (2011) Half a century of measurements of glaciers on Axel Heiberg Island, Nunavut, Canada. *Arctic*, 371–375 (doi: 10.14430/arctic4127)

Cogley JG, Adams W, Ecclestone M, Jung-Rothenhäusler F and Ommanney C (1996) Mass balance of white glacier, Axel Heiberg Island, N.W.T., Canada, 1960–91. *Journal of Glaciology*, **42**(142), 548–563 (doi: 10.3189/s0022143000003531)

Colgan W, Rajaram H, Abdalati W, McCutchan C, Mottram R, Moussavi MS and Grigsby S (2016) Glacier crevasses: Observations, models, and mass balance implications: Glacier crevasses. *Reviews of Geophysics*, **54**(1), 119–161 (doi: 10.1002/2015rg000504)

Cuffey KM and Paterson WSB (2010) *The physics of glaciers*. Academic Press

Cumming IG and Zhang J (1999) Measuring the 3-D flow of the Lowell Glacier with InSAR. *Proceedings of ESA Fringe*, **99**

De Zan F (2014) Accuracy of incoherent speckle tracking for circular gaussian signals. *IEEE Geoscience and Remote Sensing Letters*, **11**(1), 264–267 (doi: 10.1109/lgrs.2013.2255259)

Esri (2022) 'World Imagery' [basemap]. 15 m scale. Available at `www.arcgis.com/home/item.html?id=10df2279f9684e4a9f6a7f08febac2a9` (September 23, 2022)

Eyles N and Rogerson R (1977) Glacier movement, ice structures, and medial moraine form at a glacier confluence, Berendon Glacier, British Columbia, Canada. *Canadian Journal of Earth Sciences*, **14**(12), 2807–2816

Faillettaz J, Funk M and Vincent C (2015) Avalanching glacier instabilities: Review on processes and early warning perspectives. *Reviews of Geophysics*, **53**(2), 203–224

Farinotti D, Huss M, Fürst JJ, Landmann J, Machguth H, Maussion F and Pandit A (2019) A consensus estimate for the ice thickness distribution of all glaciers on Earth. *Nature Geoscience*, **12**(3), 168–173 (doi: 10.1038/s41561-019-0300-3)

Fatland DR and Lingle CS (2002) InSAR observations of the 1993–95 Bering Glacier (Alaska, USA) surge and a surge hypothesis. *Journal of Glaciology*, **48**(162), 439–451 (doi: 10.3189/172756502781831296)

Ferguson R (1973) Sinuosity of supraglacial streams. *Geological Society of America Bulletin*, **84**(1), 251–256 (doi: 10.1130/0016-7606(1973)84<251:soss>2.0.co;2)

Gardner AS, Moholdt G, Scambos T, Fahnstock M, Ligtenberg S, den Broeke MV and Nilsson J (2018) Increased west antarctic and unchanged east antarctic ice discharge over the last 7 years. *The Cryosphere*, **12**(2), 521–547 (doi: 10.5194/tc-12-521-2018)

Gardner AS, Fahnestock M and Scambos T (2022) Measures its_live regional glacier and ice sheet surface velocities, version 1 (doi: 10.5067/6II6VW8LLWJ7)

Geuzaine C and Remacle JF (2009) Gmsh: A 3-d finite element mesh generator with built-in pre-and post-processing facilities. *International journal for numerical methods in engineering*, **79**(11), 1309–1331 (doi: 10.1002/nme.2579)

Glasser NF and Gudmundsson G (2012) Longitudinal surface structures (flowstripes) on Antarctic glaciers. *The Cryosphere*, **6**(2), 383–391 (doi: 10.5194/tc-6-383-2012)

Goldstein RM, Engelhardt H, Kamb B and Frolich RM (1993) Satellite radar interferometry for monitoring ice sheet motion: application to an Antarctic ice stream. *Science*, **262**(5139), 1525–1530 (doi: 10.1126/science.262.5139.1525)

Gray AL, Mattar K, Vachon P, Bindschadler R, Jezek K, Forster R and Crawford J (1998) InSAR results from the RADARSAT Antarctic Mapping Mission data: estimation of glacier motion using a simple registration procedure. In *IGARSS'98. Sensing and Managing the Environment. 1998 IEEE International Geoscience and Remote Sensing. Symposium Proceedings.(Cat. No. 98CH36174)*, volume 3, 1638–1640, IEEE (doi: 10.4095/219342)

Gray AL, Short NH, Mattar K and Jezek K (2001) Velocities and flux of the Filchner ice shelf and its tributaries determined from speckle tracking interferometry. *Canadian Journal of Remote Sensing*, **27**(3), 193–206 (doi: 10.4095/219822)

Hambrey MJ (1977) Supraglacial drainage and its relationship to structure, with particular reference to charles rabots bre, okstindan, norway. *Norsk Geografisk Tidsskrift - Norwegian Journal of Geography*, **31**(2), 69–77 (doi: 10.1080/00291957708545319)

Hambrey MJ and Müller F (1978) Structures and ice deformation in the White Glacier, Axel Heiberg Island, Northwest Territories, Canada. *Journal of Glaciology*, **20**(82), 41–66 (doi: 10.1017/s0022143000021213)

Irvine-Fynn TD, Hodson AJ, Moorman BJ, Vatne G and Hubbard AL (2011) Polythermal glacier hydrology: a review. *Reviews of Geophysics*, **49**(4) (doi: 10.1029/2010rg000350)

Isenko E, Naruse R and Mavlyudov B (2005) Water temperature in englacial and supraglacial channels: Change along the flow and contribution to ice melting on the channel wall. *Cold regions science and technology*, **42**(1), 53–62 (doi: 10.1016/j.coldregions.2004.12.003)

Joughin I (2002) Ice-sheet velocity mapping: a combined interferometric and speckle-tracking approach. *Annals of Glaciology*, **34**, 195–201 (doi: 10.3189/172756402781817978)

Joughin I, Smith BE and Abdalati W (2011) Glaciological advances made with interferometric synthetic aperture radar. *Journal of Glaciology*, **56**(200), 1026–1042 (doi: 10.3189/002214311796406158)

Joughin I, Smith BE and Howat IM (2018) A complete map of Greenland ice velocity derived from satellite data collected over 20 years. *Journal of Glaciology*, **64**(243), 1–11 (doi: 10.1017/jog.2017.73)

Kaiser HF and Dickman K (1962) Sample and population score matrices and sample correlation matrices from an arbitrary population correlation matrix. *Psychometrika*, **27**(2), 179–182 (doi: 10.1007/bf02289635)

Kobayashi T, Morishita Y and Yarai H (2018) SAR-revealed slip partitioning on a bending fault plane for the 2014 northern Nagano earthquake at the northern Itoigawa–Shizuoka tectonic line. *Tectonophysics*, **733**, 85–99 (doi: 10.1016/j.tecto.2017.12.001)

Lee JS (1983) A simple speckle smoothing algorithm for synthetic aperture radar images. *IEEE Transactions on Systems, Man, and Cybernetics*, (1), 85–89 (doi: 10.1109/tsmc.1983.6313036)

Maag HU (1963) Marginal drainage and glacier-dammed lakes

Magnard C, Werner C and Wegmuller U (2017) GAMMA Technical Report: Offset estimation programs update. Technical report

MDA (2018) RADARSAT-2 product description. Technical report, Available at `https://earth.esa.int/eogateway/documents/20142/0/Radarsat-2-Product-description.pdf/f2783c7b-6a22-cbe4-f4c1-6992f9926dca`

Michel R and Rignot E (1999) Flow of Glaciar Moreno, Argentina, from repeat-pass Shuttle Imaging Radar images: comparison of the phase correlation method with radar interferometry. *Journal of Glaciology*, **45**(149), 93–100 (doi: 10.3189/s0022143000003075)

Millan R, Mouginot J, Rabatel A and Morlighem M (2022) Ice velocity and thickness of the world's glaciers. *Nature Geoscience*, **15**(2), 124–129 (doi: 10.1038/s41561-021-00885-z)

Minchew B, Simons M, Björnsson H, Pálsson F, Morlighem M, Seroussi H, Larour E and Hensley S (2016) Plastic bed beneath Hofsjökull ice cap, central Iceland, and the sensitivity of ice flow to surface meltwater flux. *Journal of Glaciology*, **62**(231), 147–158 (doi: 10.1017/jog.2016.26)

Mohammadimanesh F, Salehi B, Mahdianpari M, Brisco B and Motagh M (2018) Multi-temporal, multi-frequency, and multi-polarization coherence and SAR backscatter analysis of wetlands. *ISPRS Journal of Photogrammetry and Remote Sensing*, **142**, 78–93 (doi: 10.1016/j.isprsjprs.2018.05.009)

Monz ME, Hudleston PJ, Cook SJ, Zimmerman T and Leng MJ (2022) Thrust faulting in glaciers? re-examination of debris bands near the margin of Storglaciären, Sweden. *Boreas*, **51**(1), 78–99 (doi: 10.1111/bor.12549)

Moore PL, Iverson NR and Cohen D (2010) Conditions for thrust faulting in a glacier. *Journal of Geophysical Research: Earth Surface*, **115**(F2) (doi: 10.1029/2009jf001307)

Moreira A, Prats-Iraola P, Younis M, Krieger G, Hajnsek I and Papathanassiou KP (2013) A tutorial on synthetic aperture radar. *IEEE Geoscience and Remote Sensing Magazine*, **1**(1), 6–43 (doi: 10.1109/mgrs.2013.2248301)

Morena L, James K and Beck J (2004) An introduction to the RADARSAT-2 mission. *Canadian Journal of Remote Sensing*, **30**(3), 221–234 (doi: 10.5589/m04-004)

Müller F (1962) Zonation in the accumulation area of the glaciers of Axel Heiberg Island, N.W.T., Canada. *Journal of Glaciology*, **4**(33), 302–311, ISSN 0022-1430, 1727-5652 (doi: 10.3189/s0022143000027623)

Nye JF (1965) The flow of a glacier in a channel of rectangular, elliptic or parabolic cross-section. *Journal of glaciology*, **5**(41), 661–690 (doi: 10.3189/s0022143000018670)

Pepe A and Calò F (2017) A review of interferometric synthetic aperture RADAR (InSAR) multi-track approaches for the retrieval of Earth's surface displacements. *Applied Sciences*, **7**(12), 1264 (doi: 10.3390/app7121264)

Porter C, Morin P, Howat I, Noh MJ, Bates B, Peterman K, Keesey S, Schlenk M, Gardiner J, Tomko K, Willis M, Kelleher C, Cloutier M, Husby E, Foga S, Nakamura H, Platson M, Wethington J Michael, Williamson C, Bauer G, Enos J, Arnold G, Kramer W, Becker P, Doshi A, D'Souza C, Cummens P, Laurier F and Bojesen M (2018) ArcticDEM (doi: 10.7910/DVN/OHHUKH)

Rabus B (2017) An example of discontinuous polythermal ice dynamics observed with high resolution InSAR, Thompson/White Glaciers, Canadian Arctic. Presented at the annual meeting of Northwest Glaciologists, 2017

Rabus B and Echelmeyer KA (1997) The flow of a polythermal glacier: McCall Glacier, Alaska, U.S.A. *Journal of Glaciology*, **43**(145), 522–536 (doi: 10.3189/s0022143000035139)

Rabus BT and Lang O (2002) On the representation of ice-shelf grounding zones in SAR interferograms. *Journal of Glaciology*, **48**(162), 345–356 (doi: 10.3189/172756502781831197)

Rathgeber F, Ham DA, Mitchell L, Lange M, Luporini F, McRae AT, Bercea GT, Markall GR and Kelly PH (2016) Firedrake: automating the finite element method by composing abstractions. *ACM Transactions on Mathematical Software (TOMS)*, **43**(3), 1–27 (doi: 10.1145/2998441)

Rignot E (1998) Fast recession of a West Antarctic glacier. *Science*, **281**(5376), 549–551 (doi: 10.1126/science.281.5376.549)

Shapero DR, Badgeley JA, Hoffman AO and Joughin I (2021) icepack: A new glacier flow modeling package in python, version 1.0. *Geoscientific Model Development*, **14**(7), 4593–4616 (doi: 10.5194/gmd-14-4593-2021)

St Germain SL and Moorman BJ (2019) Long-term observations of supraglacial streams on an Arctic glacier. *Journal of Glaciology*, **65**(254), 900–911 (doi: 10.1017/jog.2019.60)

Thomson LI and Copland L (2017) Multi-decadal reduction in glacier velocities and mechanisms driving deceleration at polythermal White Glacier, Arctic Canada. *Journal of Glaciology*, **63**(239), 450–463 (doi: 10.1017/jog.2017.3)

Thomson LI, Zemp M, Copland L, Cogley J and Ecclestone MA (2017) Comparison of geodetic and glaciological mass budgets for White Glacier, Axel Heiberg Island, Canada. *Journal of Glaciology*, **63**(237), 55–66, ISSN 0022-1430, 1727-5652 (doi: 10.1017/jog.2016.112)

Van Wychen W, Copland L, Jiskoot H, Gray AL, Sharp M and Burgess D (2018) Surface velocities of glaciers in western canada from speckle-tracking of ALOS PALSAR and RADARSAT-2 data. *Canadian Journal of Remote Sensing*, **44**(1), 57–66 (doi: 10.1080/07038992.2018.1433529)

Wang Q, Fan J, Zhou W, Tong L, Guo Z, Liu G, Yuan W, Sousa JJ and Perski Z (2019) 3D surface velocity retrieval of mountain glacier using an offset tracking technique applied to ascending and descending SAR constellation data: a case study of the Yiga Glacier. *International Journal of Digital Earth*, **12**(6), 614–624 (doi: 10.1080/17538947.2018.1470690)

Weertman J (1957) On the sliding of glaciers. *Journal of glaciology*, **3**(21), 33–38 (doi: 10.3189/s0022143000024709)

Wilson N, Flowers G and Mingo L (2013) Comparison of thermal structure and evolution between neighboring subarctic glaciers. *Journal of Geophysical Research: Earth Surface*, **118**(3), 1443–1459 (doi: 10.1002/jgrf.20096)

Xie H, Pierce LE and Ulaby FT (2002) Statistical properties of logarithmically transformed speckle. *IEEE transactions on geoscience and remote sensing*, **40**(3), 721–727 (doi: 10.1109/tgrs.2002.1000333)

Yoo JC and Han TH (2009) Fast normalized cross-correlation. *Circuits, Systems and Signal Processing*, **28**(6), 819–843 (doi: 10.1007/s00034-009-9130-7)

Yu H, Lan Y, Yuan Z, Xu J and Lee H (2019) Phase unwrapping in InSAR: A review. *IEEE Geoscience and Remote Sensing Magazine*, **7**(1), 40–58 (doi: 10.1109/MGRS.2018.2873644)